J. Fluid Mech. (1990), *vol.* 211, *pp.* 515–528
Printed in Great Britain

A jet in crossflow. Part 2

By D. J. NEEDHAM[1], N. RILEY[1], C. C. LYTTON[2] AND J. H. B. SMITH[2]

[1] School of Mathematics, University of East Anglia, Norwich NR4 7TJ, UK

[2] Aerodynamics Department, Royal Aerospace Establishment, Farnborough GU14 6TD, UK

(Received 24 February 1989)

A recent paper by Needham, Riley & Smith (1988) considers the flow of a jet of inviscid, incompressible fluid emerging from a circular pipe into a weak crossflow. In this paper we extend their results. In particular we show how the Kutta condition at the pipe lip may be satisfied, and we present details of the flow field obtained from both the formal solution and a field calculation.

1. Introduction

In a recent paper, Needham, Riley & Smith (1988, herein referred to as I), we reported an investigation aimed at identifying an inviscid mechanism for the deflection of a jet in crossflow. In it a formal solution is presented to the problem of a jet emerging from a cylindrical pipe of circular cross-section into an inclined ambient flow, for the idealized case of an inviscid, incompressible fluid in steady, irrotational flow. A small-disturbance treatment is applied, assuming that the component of the velocity of the ambient flow normal to the pipe axis is small compared with the jet speed, and that the departure of the jet boundary from the cylindrical prolongation of the pipe is small. The solution obtained is such as to violate this latter assumption sufficiently far downstream from the pipe orifice, however small the crossflow. We are still unable to improve upon this shortcoming, for which the fully three-dimensional elliptic free-boundary problem would have to be attacked, but we have improved the treatment in two respects.

Most importantly, we have found a solution that satisfies a Kutta condition at the lip of the pipe. The solution found in I for the flow on the lengthscale of the pipe diameter involves a singular behaviour at the lip where the stream-surface boundary condition on the pipe gives way to a pressure-continuity boundary condition on the jet surface. The consequences of this have been explored by Lytton & Smith (1988), some of which is now irrelevant. The singularity is here eliminated by the introduction of an eigensolution in the far-field solution of I, the existence of which only becomes apparent when the series expansions of I are carried to higher order. The effect of this is to introduce a free parameter in the solution close to the lip, the choice of which enables the singularity there to be removed. The inclusion of this eigensolution in the far-field solution is simply equivalent to a change of origin; its presence obviates the need, conjectured in I, to solve a nonlinear problem close to the orifice lip. The principal conclusion of I, that the jet is deflected downstream if and only if there is a component of the ambient flow parallel to the pipe axis (a coflow), is thus unaffected. Coelho & Hunt (1989) consider a jet emerging normally from a plane wall, so that the coflow is zero. They find there is no deflection when the flow is inviscid, in agreement with this conclusion.

We are also now able to present the solution near the pipe orifice in graphical form. The analytical solution is still expressed in the form of complicated integrals, essentially unchanged from I. The evaluation of some of these expressions has been undertaken by Lytton & Smith (1988) for $\lambda = 1$, where λ is the ratio of the speed of the coflow to that in the pipe, far from the orifice. This evaluation has now been extended to the range $0 \leqslant \lambda < 1$. In addition, for the flow near the orifice, the potential-flow problems inside and outside the cylinder which represents the pipe and jet boundary, coupled on the jet boundary, have been solved numerically using a finite-difference approximation. The agreement between the analytical and numerical solutions is reassuring and several of the flow features revealed are of interest.

In §2 of this paper we briefly summarize the results of I, and show how they may be extended to eliminate the singularity at the lip of the pipe. Section 3 contains a discussion of the methods used to provide numerical information about the flow near the orifice: first to evaluate the analytical expressions and secondly to solve a finite-difference approximation to the governing partial differential equations. In §4 we present and discuss various features of the flow revealed by this numerical solution, and in §5 we list our main conclusions. The discussion in I of the physical aspects of the problem and of the implications of the solution remains valid and so is not repeated here.

2. Equations and solution procedure

Our development of the solution outlined in this section follows very closely the treatment in I, and will need to be read in conjunction with that paper.

Fluid emerges with mean speed U_0 from the pipe orifice. The pipe is at angle $\tan^{-1}(\epsilon/\lambda)$ to the undisturbed outer flow direction, whose speed is $U_0(\lambda^2+\epsilon^2)^{\frac{1}{2}}$ with λ arbitrary and $\epsilon \ll 1$. The undisturbed pressure outside the pipe, $\bar{p}_\infty$, and within it, $\bar{p}_{-\infty}$, are related by (I2.1)†, with $\alpha = 0$ as subsequently required in I. Flow variables are made dimensionless as in I and velocity potentials $\varphi, \tilde{\varphi}$ are introduced for the inner and outer flows respectively, which satisfy Laplace's equation (I2.2). Boundary conditions at the pipe surface, and at the jet surface, are as given by (I2.3), (I2.4) and (I2.5) respectively, with the far-field conditions given by (I2.6), (I2.7). The potentials $\varphi, \tilde{\varphi}$ and the jet-shape function F are expanded as

$$\varphi = \frac{\lambda\xi}{\epsilon} + \epsilon\lambda\{\varphi_{11}(r,\theta) + \xi\varphi_{12}(r,\theta) + \xi^2\varphi_{13}(r,\theta) + \ldots\} + \epsilon^2\{\varphi_{21}(r,\theta) + \xi\varphi_{22}(r,\theta) + \ldots\} + O(\epsilon^3), \quad (2.1)$$

$$\tilde{\varphi} = \frac{\xi}{\epsilon} + \epsilon\{\xi\tilde{\varphi}_{12}(r,\theta) + \xi^2\tilde{\varphi}_{13}(r,\theta) + \ldots\} + \epsilon^2\{\tilde{\varphi}_{21}(r,\theta) + \xi\tilde{\varphi}_{22}(r,\theta) + \ldots\} + O(\epsilon^3), \quad (2.2)$$

$$F = r - 1 - \xi^2 f_2(\theta) - \xi^3 f_3(\theta) + \ldots + \epsilon\{\xi f_c(\theta) + \ldots\} + O(\epsilon^2), \quad (2.3)$$

where $\xi = \epsilon x$ is the far-field coordinate of I, and (r, θ, x) are cylindrical polar coordinates with θ measured from the leeward generator of the pipe (cf. figure 1 of I). These expressions differ from the expansions (I3.5)–(I3.7) by the inclusion of terms $O(\epsilon^2)$ in (2.1), (2.2) and $O(\epsilon)$ in (2.3). In I the coefficients of the terms $O(\epsilon)$ in

† (I2.1) denotes equation (2.1) of I.

(2.1), (2.2) and $O(1)$ in (2.3) were determined by substitution of the expansions into (I2.2)–(I2.7) and equating coefficients of powers of ξ. The results obtained are set out in I. We move now to the additional terms in (2.1)–(2.3), whose inclusion does not affect the far-field discussion in I. If we follow the same procedure and note that the pressure condition (I2.5) at $O(\epsilon^3)$ is to be interpreted as a condition on $\varphi_{22}, \tilde{\varphi}_{22}$, then for $\varphi_{21}, \tilde{\varphi}_{21}$ we have

$$\nabla^2 \varphi_{21} = \nabla^2 \tilde{\varphi}_{21} = 0 \tag{2.4}$$

with, from (I2.4)

$$\varphi_{21r} = \lambda f_c, \quad \tilde{\varphi}_{21r} = f_c, \quad \text{or} \quad \varphi_{21r} = \lambda \tilde{\varphi}_{21r} \quad \text{on} \quad r = 1, \tag{2.5}$$

together with conditions that the solutions remain finite as $r \to 0, \infty$. The conditions imposed on $\varphi_{21}, \tilde{\varphi}_{21}$ are not sufficient to render them unique, and they thus assume the role of eigensolutions on the scale of ξ. If we anticipate the appropriate angular dependence as $\cos 2\theta$ then

$$\varphi_{21} = \frac{c\lambda}{1+\lambda^2} \frac{\cos 2\theta}{r^2}, \quad \tilde{\varphi}_{21} = -\frac{c}{1+\lambda^2} r^2 \cos 2\theta, \quad f_c = -\frac{2c}{1+\lambda^2} \cos 2\theta. \tag{2.6}$$

The constant c in (2.6) is not determined at this stage.

We turn next to the near-field solution with $x = O(1)$. Correct to $O(\epsilon^2)$ we write φ, $\tilde{\varphi}$ as in (I3.23). Each of the unknowns $\psi, \tilde{\psi}$ satisfies (I2.2) together with (I3.24), (I3.25) in the far field, (I3.27) at the pipe surface and (I3.28*a*, *b*), with $\alpha = 0$, at the jet surface. Matching with the far-field solution now requires

$$\psi \sim \frac{\lambda}{1+\lambda^2} \frac{x+c}{r^2} \cos 2\theta, \quad \tilde{\psi} \sim -\frac{1}{1+\lambda^2} (x+c) r^2 \cos 2\theta \quad \text{as} \quad x \to \infty, \tag{2.7}$$

in place of (I3.26). We note that the θ-dependence of $\psi, \tilde{\psi}$ will be represented completely by a factor $\cos 2\theta$.

The problem posed above for the neighbourhood of the pipe orifice differs from that in I only by the inclusion of the arbitrary constant c in (2.7). We see that the introduction of the eigensolutions $\varphi_{21}, \tilde{\varphi}_{21}$ in the solution on the larger lengthscale corresponds to a shift of origin in the near-field solution.

The method of solution for $\psi, \tilde{\psi}$, by the Wiener–Hopf technique follows exactly as in I with x replaced by $x+c$ in the boundary conditions where appropriate. Fourier transforms are defined exactly as in I, but now the transformed quantities contain factors $e^{\pm \delta c}$ (δ is an arbitrary small parameter as introduced in I) as appropriate. The following Wiener–Hopf equation results (cf. I B12):

$$\bar{K}(s)\, \bar{\eta}_+ + \bar{\eta}_- = \frac{i e^{-\delta c}}{2\delta(s+i\delta)} + \frac{i\bar{K}(s)\, e^{\delta c}}{(1+\lambda^2)\, \delta(s-i\delta)}, \tag{2.8}$$

where s is the transform variable and $\bar{K}, \bar{\eta}_+, \bar{\eta}_-$ are exactly as in I. Thus $\bar{K}_+(s), \bar{K}_-(s)$, the multiplicative factors of the kernel $\bar{K}(s) = \bar{K}_+(s)\, \bar{K}_-(s)$, are as in I and we again have $\bar{K}_+(i\delta) = \bar{K}_-(-i\delta)$. The subsequent analysis of I for the transforms of our potential functions follows through, except that $\bar{K}_\pm(\pm i\delta)$ is replaced everywhere by $e^{\delta c} \bar{K}_\pm(\pm i\delta)$. This modification is crucial as taking the limit $\delta \to 0$ shows. Thus

$$e^{\delta c} \bar{K}_\pm(\pm i\delta) = \left(\frac{1+\lambda^2}{2}\right)^{\frac{1}{2}} \{1 + (A+c)\, \delta\} + O(\delta^2). \tag{2.9}$$

In (2.9) A is a property of $\bar{K}_{\pm}(\pm \mathrm{i}\delta)$ given by

$$A = \frac{(1+\lambda^2)^{\frac{1}{2}}}{2^{\frac{3}{2}}\pi} \int_0^\infty \frac{\mathrm{i}\hat{K}(p)\, J_2'(p)\, \bar{K}_+(\mathrm{i}p)}{p} \mathrm{d}p, \tag{2.10}$$

where $\hat{K}(p)$ is a complicated expression involving modified Bessel functions of the first and second kind, of order two, given by (I B19), and J_2 is the Bessel function of the first kind of order two. Equation (2.10) for A is as in I, except that subsequent analysis has allowed a complicated integral to be replaced by a simple expression.

The result (2.9) shows that expressions (I B22a, b), (I B23a, b) for the potential function, in each of the four regions $r \gtrless 1$, $x \gtrless 0$, are unchanged except that A must be replaced by $A+c$, and the terms that are linear in x in the potential by $x+c$, as in (2.11) below. From this observation an important conclusion follows. If we evaluate the velocity components at the lip of the orifice, that is on $r = 1$ as $x \to 0+$, we find

$$\frac{\partial \tilde{\psi}}{\partial r} \sim -\frac{\sqrt{2}\,(A+c)\cos 2\theta}{(1+\lambda^2)\,\pi^{\frac{1}{2}}} x^{-\frac{1}{2}}, \quad \frac{\partial \psi}{\partial r} \sim -\frac{\sqrt{2}\,\lambda(A+c)\cos 2\theta}{(1+\lambda^2)\,\pi^{\frac{1}{2}}} x^{-\frac{1}{2}}, \tag{2.11}$$

with $\partial\tilde{\psi}/\partial x, \partial\psi/\partial x$ bounded. We now see that it is possible to satisfy a Kutta condition at the lip by the choice $c = -A$.

This removes an unsatisfactory feature from I. The larger-scale solution of that earlier paper is unaffected to the order it is taken. But the inclusion of the eigensolution (2.6) at higher order in the far-field solution does have a significant effect upon the solution close to the pipe orifice. With the choice $c = -A$, which enables us to satisfy the Kutta condition at $r = 1, x = 0$, the solutions, and their asymptotic forms, in (I3.36)–(I3.43) become

(i) $x \leqslant 0, r \leqslant 1$

$$\tilde{\psi}(r,\theta,x) = \frac{\sqrt{2}\cos 2\theta}{(1+\lambda^2)^{\frac{1}{2}}} \sum_{n=1}^{\infty} \frac{J_2(\Omega_n r)\, \mathrm{e}^{-\Omega_n |x|}}{\Omega_n^3 \bar{K}_+(\mathrm{i}\Omega_n)\, J_2''(\Omega_n)}, \tag{2.12a}$$

$$\tilde{\psi}(r,\theta,x) \sim \frac{\sqrt{2}\, J_2(\Omega_1 r)\, \mathrm{e}^{-\Omega_1 |x|} \cos 2\theta}{(1+\lambda^2)^{\frac{1}{2}} \Omega_1^3 \bar{K}_+(\mathrm{i}\Omega_1)\, J_2''(\Omega_1)} \quad \text{as} \quad x \to -\infty, \tag{2.12b}$$

where Ω_n are the positive zeros of $J_2'(\Omega)$.

(ii) $x \geqslant 0, r \leqslant 1$

$$\tilde{\psi}(r,\theta,x) = -\frac{(x+c)\, r^2 \cos 2\theta}{1+\lambda^2} - \frac{\mathrm{i}\cos 2\theta}{\sqrt{2}\,\pi(1+\lambda^2)^{\frac{1}{2}}} \int_0^\infty \frac{\hat{K}(p)\, J_2(pr)\, \bar{K}_-(-\mathrm{i}p)}{p^2} \mathrm{e}^{-px} \mathrm{d}p, \tag{2.12c}$$

$$\tilde{\psi}(r,\theta,x) \sim -\frac{(x+c)\, r^2 \cos 2\theta}{1+\lambda^2} \left\{ 1 - \frac{\lambda^2}{8(1+\lambda^2)\, x^4} \right\} \quad \text{as} \quad x \to \infty. \tag{2.12d}$$

(iii) $x \leqslant 0, r \geqslant 1$

$$\psi(r,\theta,x) = -\frac{\lambda \cos 2\theta}{\sqrt{2}\,\pi(1+\lambda^2)^{\frac{1}{2}}} \int_0^\infty \left\{ \frac{K_2(\mathrm{i}pr)}{K_2'(\mathrm{i}p)} + \frac{K_2(-\mathrm{i}pr)}{K_2'(-\mathrm{i}p)} \right\} \frac{\mathrm{e}^{-p|x|}}{p^3 \bar{K}_+(\mathrm{i}p)} \mathrm{d}p, \tag{2.12e}$$

$$\psi(r,\theta,x) \sim -\frac{\lambda(r^4+1)\cos 2\theta}{16 r^2 x^2 (1+\lambda^2)} \quad \text{as} \quad x \to -\infty, \quad r \text{ fixed}. \tag{2.12f}$$

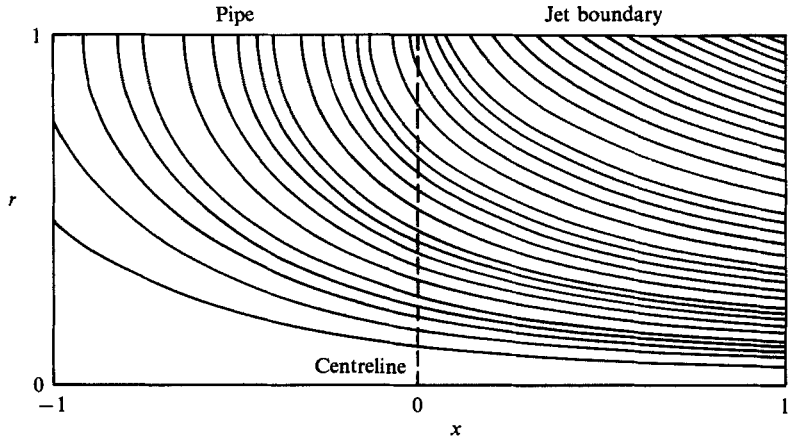

FIGURE 1. Contours of $\tilde{\psi}^*$ near the orifice for $\lambda = 1$.

(iv) $x \geqslant 0, r \geqslant 1$

$$\psi(r,\theta,x) = \frac{\lambda(x+c)\cos 2\theta}{(1+\lambda^2)r^2} - \frac{\lambda\cos 2\theta}{\sqrt{2\pi}(1+\lambda^2)^{\frac{1}{4}}}\int_0^\infty \left\{\frac{iK_2(ipr)}{I_2(ip)K_2'(ip)-\lambda^2K_2(ip)I_2'(ip)}\right.$$
$$\left. + \frac{iK_2(-ipr)}{I_2(ip)K_2'(-ip)+\lambda^2K_2(-ip)I_2'(ip)}\right\}\frac{\bar{K}_-(-ip)I_2'(ip)\,e^{-px}}{p^2}\,dp, \quad (2.12g)$$

$$\psi(r,\theta,x) \sim \frac{\lambda(x+c)\cos 2\theta}{(1+\lambda^2)r^2}\left\{1+\frac{(1-\lambda^2)(1+\lambda^2)^{-1}+r^4}{16x^4}\right\} \quad \text{as} \quad x\to\infty, \quad r \text{ fixed}, \quad (2.12h)$$

where $c = -A$ throughout.

3. Numerical techniques

3.1. *Evaluation of analytical expressions representing the flow field*

For the flow near the pipe orifice, the outcome of the analysis in both I and the present paper is a number of infinite series and integrals. Considerable care is needed in their numerical evaluation, so an indication of the methods used is included here.

For $\lambda = 1$, for which some simplification occurs, Lytton & Smith (1988) present an evaluation of some of the expressions in I, including that for the important parameter A. We have repeated these calculations for the present expressions. Sufficient accuracy was obtained when the series for the flow inside the pipe was summed over the first 400 zeros of J_2' and Richardson extrapolation used on the partial sums, and when, for the flow in the jet, the integration extended over $0 \leqslant p \leqslant 800$, with ten integration points in each unit sub-interval, making 8000 in all.

Figure 1 shows a contour plot of the function $\tilde{\psi}^*(r,x)$ where

$$\tilde{\psi} = \tilde{\psi}^*(r,x)\cos 2\theta. \quad (3.1)$$

The contours are not at equal intervals, because we wish to represent the flow some distance into the pipe, where the disturbance velocity is small, as well as in the jet, where it is large. With $\tilde{\psi} = 0$ on the centreline, the contours are at

$$0(0.002)\,0.01(0.004)\,0.03(0.008)\,0.07(0.016)\,0.15(0.032)\,0.598.$$

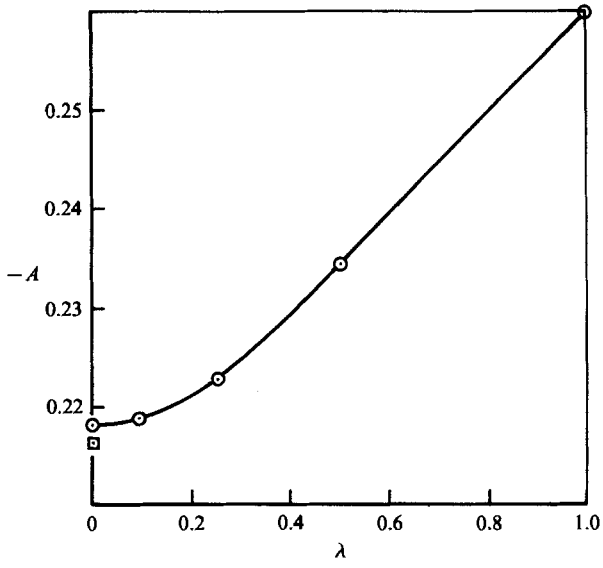

FIGURE 2. Variation of A with λ: ⊙, present; ⊡, Coelho & Hunt (1989).

The four discontinuities in the interval are apparent. Note that the contours are normal to the pipe, consistent with the vanishing of the normal velocity; the spacing is even at the pipe lip, consistent with the Kutta condition there; and the contours are continuous and smooth across the orifice plane, confirming the validity and accuracy of the solution. The corresponding plots in Lytton & Smith (1988), based on I, show a distinct local structure near the lip, with the contour spacing decreasing to zero, and some of the contours that originate in the pipe subsequently crossing the jet boundary.

We now turn to the evaluation of A for smaller values of λ. It emerges that for small values of λ the integrand in (2.10) has peaks at the zeros, χ_n, of J_2, so using equal sub-intervals for the integration is inefficient. Instead, the basic sub-interval is chosen to be that between a zero of J_2 and a zero of J_2', and an adaptive integration scheme is used within each of these sub-intervals. The scheme is designed to integrate accurately away from χ_n until the integrand becomes negligibly small. Then, with $A(N)$ denoting the value of A calculated in this way using N zeros of J_2, we assume an asymptotic expression

$$A(N) = A + \frac{\alpha_1}{N^{\frac{1}{2}}} + \frac{\alpha_2}{N^{\frac{3}{2}}} \tag{3.2}$$

and determine α_1, α_2 and A by using $A(N)$, $A(N-100)$ and $A(N-200)$. For $\lambda \geqslant 0.5$, $N = 2000$ is adequate; for smaller λ, $N = 4000$ is used. For $\lambda = 0$, the integrand resembles a series of delta-functions and the integral can be shown to reduce to an infinite sum, giving

$$A(\lambda = 0) = \frac{1}{\sqrt{2}} \sum_{n=1}^{\infty} \frac{\bar{K}_+(\mathrm{i}\chi_n)}{\chi_n}. \tag{3.3}$$

We evaluated this sum up to $n = 4000$ and then used Richardson extrapolation on the partial sums to estimate the sum to infinity. The values of A obtained in these ways are shown in figure 2. In the present solution, as in I, λ appears as a factor in

the expressions for the axial component of the velocity outside the pipe and jet, so the present solution with $\lambda = 0$ is a solution to the inviscid problem of Coelho & Hunt (1989), taken to the same order in ϵ. In that paper C_2 corresponds to the present A and their value is shown in figure 2 for comparison. In view of the entirely different analytical and numerical procedures used, the close agreement is encouraging. Regarding A as an origin shift for the axial coordinate, as indicated in §2, we see that its value is significant, on the scale of the pipe diameter, but its variation with λ is small.

3.2. *Direct calculation of the flow field*

In order to provide an independent check on some of the results obtained by the methods of §3.1, and to determine further details of the flow field (in particular for $r > 1$), we have made a direct numerical attack upon Laplace's equation (I2.2), subject to the boundary conditions (I3.24), (I3.25), (I3.27), (I3.28) and (2.7). Because of the form of the boundary conditions (2.7) we have chosen to work with the perturbations $u = \psi_x$, $\tilde{u} = \tilde{\psi}_x$ to the axial velocities, rather than the potentials directly. Each of $u, \tilde{u}$ satisfies (I2.2). We also transform the infinite flow-field domain into the finite computational domain $-1 \leqslant X \leqslant 1$, $0 \leqslant R \leqslant 1$, where the new variables are defined by

$$x = \tan \tfrac{1}{2}\pi X, \quad r = \tan \tfrac{1}{2}\pi R. \tag{3.4}$$

If we further write $u = U(R, X)\cos 2\theta$, $\tilde{u} = \tilde{U}(R, X)\cos 2\theta$ then U satisfies the equation

$$\sin^2 \pi R \frac{\partial^2 U}{\partial R^2} + \tfrac{1}{2}\pi \sin 2\pi R \frac{\partial U}{\partial R} + 4 \tan^2 \tfrac{1}{2}\pi R \cos^4 \tfrac{1}{2}\pi X \frac{\partial^2 U}{\partial X^2}$$
$$- 2\pi \sin \pi X \cos^2 \tfrac{1}{2}\pi X \tan^2 \tfrac{1}{2}\pi R \frac{\partial U}{\partial X} - 4\pi^2 U = 0, \tag{3.5}$$

an equation which is similarly satisfied by $\tilde{U}$. The boundary conditions (I3.24), (I3.25), (2.7), (I3.27) and (I3.28) with $\alpha = 0$ now become, in turn,

$$U = 0 \quad \text{on} \quad R = 1, \quad -1 \leqslant X \leqslant 1, \tag{3.6}$$

$$U = 0 \quad \text{on} \quad X = -1, \quad \tfrac{1}{2} \leqslant R \leqslant 1, \tag{3.7}$$

$$\tilde{U} = 0 \quad \text{on} \quad X = -1, \quad 0 \leqslant R \leqslant \tfrac{1}{2}, \tag{3.8}$$

$$U = \frac{\lambda}{(1+\lambda^2)\tan^2 \tfrac{1}{2}\pi R} \quad \text{on} \quad X = 1, \quad \tfrac{1}{2} \leqslant R \leqslant 1, \tag{3.9}$$

$$\tilde{U} = -\frac{\tan^2 \tfrac{1}{2}\pi R}{1+\lambda^2} \quad \text{on} \quad X = 1, \quad 0 \leqslant R \leqslant \tfrac{1}{2}, \tag{3.10}$$

$$\frac{\partial U}{\partial R} = 0 \quad \text{on} \quad R = \tfrac{1}{2}+, \quad -1 \leqslant X \leqslant 0, \tag{3.11}$$

$$\frac{\partial \tilde{U}}{\partial R} = 0 \quad \text{on} \quad R = \tfrac{1}{2}-, \quad -1 \leqslant X \leqslant 0, \tag{3.12}$$

$$\frac{\partial U}{\partial R} - \lambda \frac{\partial \tilde{U}}{\partial R} = 0 \quad \text{on} \quad R = \tfrac{1}{2}, \quad 0 < X \leqslant 1, \tag{3.13}$$

$$\tilde{U} - \lambda U = -1 \quad \text{on} \quad R = \tfrac{1}{2}, \quad 0 < X \leqslant 1. \tag{3.14}$$

In addition to the above we take advantage of the symmetry of the problem about $r = R = 0$, so that we require

$$\frac{\partial \tilde{U}}{\partial R} = 0 \quad \text{on} \quad R = 0, \quad -1 \leqslant X \leqslant 1. \tag{3.15}$$

Our strategy is to solve (3.5), following discretization with standard central-difference formulae, using line relaxation, in each of the two regions $0 \leqslant R \leqslant \frac{1}{2}$, $|X| \leqslant 1$; $\frac{1}{2} \leqslant R \leqslant 1$, $|X| \leqslant 1$, separately. To achieve this we assign (3.13) as a boundary condition for U, and (3.14) for $\tilde{U}$ on $R = \frac{1}{2}$, $0 < X \leqslant 1$. Initially U is set to zero at each interior point and a linear variation is assumed for $\partial \tilde{U}/\partial R$ on $R = \frac{1}{2}$, $0 < X \leqslant 1$. Equation (3.5) is then solved in the upper region by successive sweeps from $X = 1$ to $X = -1$ until a prescribed convergence criterion is reached. The solution obtained is then used to estimate U on $R = \frac{1}{2}$ for use in (3.14). The equation (3.5) is then similarly solved for $\tilde{U}$ in the lower region and from that solution an updated estimate of $\partial \tilde{U}/\partial R$ at $R = \frac{1}{2}$ is obtained. This is used in (3.13) to obtain a new solution in the upper region. This procedure is continued until solutions in the upper and lower regions agree with the previously obtained solutions within some prescribed tolerance. In implementing this procedure it has been found expedient, in terms of efficiently reaching a fully converged solution, to begin with a relatively coarse convergence criterion and to reduce this gradually, following the completion of each upper and lower solution pair. In this manner we have been able to obtain solutions to any desired degree of accuracy. However, we note that in the range $0 \leqslant \lambda \leqslant 1$ converged solutions as λ approaches unity are increasingly difficult to reach. For $\lambda = 0(0.1)1.0$ we have obtained solutions for mesh size $(\delta R, \delta X) = (0.01, 0.04)$ and for $\lambda = 0, 0.5$ with mesh size $(0.005, 0.02)$.

Before leaving this section we note that by working with the perturbation velocity $\varphi_x, \tilde{\varphi}_x$ the eigenvalue c is eliminated from the boundary-value problem. For reasons which are not immediately clear the finite-difference method then selects the solution which satisfies the Kutta condition at the lip. A similar behaviour is observed in the numerical solution of the Euler equations for the compressible flow about a lifting aerofoil (see for example Lytton 1987).

4. Results

We first compare the numerical results from the totally different approaches described in §§3.1 and 3.2. Flow variations are largest near the lip, so we choose to look along the line $r = 1-, \theta = \pi$, that is, on the windward generator inside the pipe and jet, between one pipe radius upstream and downstream of the lip. The quantity shown in figure 3 is the coefficient of ϵ^2 in the axial component of the disturbance velocity, namely $\tilde{U}$ in §3.2, and the calculations are for $\lambda = 1$. The results agree in showing that the decay of the disturbance upstream in the pipe, known to be exponential from (2.12*b*), is almost complete within one pipe radius; and that the square-root behaviour at the lip expected from the analysis appears, and that the axial velocity varies slowly, but smoothly, downstream of the lip. The discrepancy between the results corresponds to an axial displacement of about 0.056, which is less than the grid spacing in the axial direction at the orifice (0.0639). Since the boundary conditions are only imposed at the grid points, there is an uncertainty of this order in the location of the lip in the finite-difference solution and greater accuracy cannot be expected. Such a degree of accuracy is regarded as acceptable and results of the

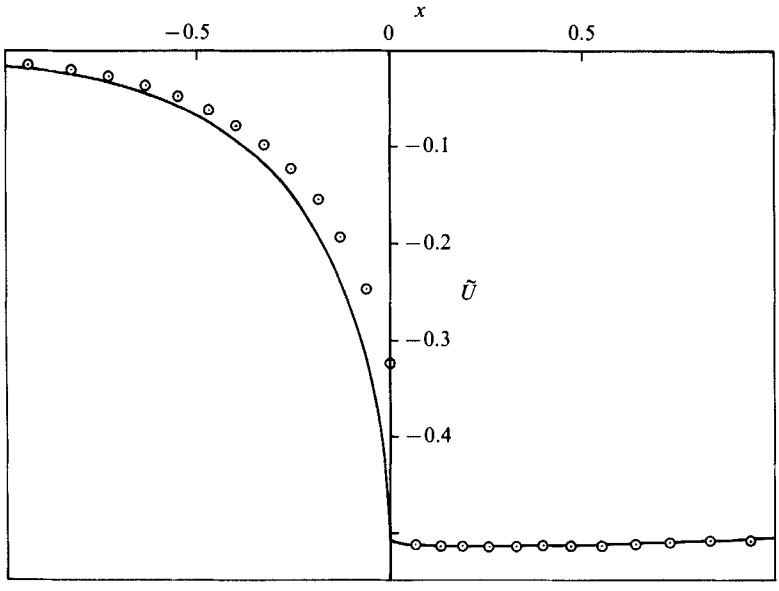

FIGURE 3. Axial component $\tilde{U}$ of disturbance velocity for $\lambda = 1$ on $r = 1-$ near the orifice: ——, analytical solution; ⊙, numerical solution.

finite-difference calculations are relied on in the remainder of this section; however, we prefer to present results obtained on the finer grid, and choose $\lambda = \frac{1}{2}$.

From (I3.23) and (2.12) it is clear that the radial component of velocity in the near field can be written as

$$\epsilon^2 v_r(r, x) \cos 2\theta. \tag{4.1}$$

v_r is shown in figure 4 as a function of x for $r = 0.5095$ (within the pipe and jet), $r = 1-$ (along the inner surfaces of the pipe and vortex sheet), $r = 1+$ (along their outer surfaces), and $r = 1.4966$ (outside the pipe and jet). On the pipe, $v_r = 0$, in accordance with the boundary condition there, and, on the vortex sheet $v_r(1-, x) = 2v_r(1+, x)$, in accordance with the kinematic boundary condition (I3.28*a*) there. The uncertainty about the position of the lip remarked on above is only half as large as in figure 3, in accordance with the finer grid. The function v_r appears to be negative everywhere, except for some very small positive values upstream in the external flow. This means that the flow is effectively inwards towards the axis when $\cos 2\theta > 0$, in the windward and leeward quadrants, and away from the axis when $\cos 2\theta < 0$, in the lateral quadrants. This is consistent with the lateral flattening of the jet which is a feature of the larger-scale solution, as discussed in I. The curves are seen to become straight to the right of figure 4, corresponding to the linearity in x of the asymptotic expressions (2.7). The asymptotic directions of these lines are specified by the boundary conditions (3.9) and (3.10), but it is remarkable that these slopes are attained within one pipe radius of the orifice. The straight line approximations to the curves provide an independent, though imprecise, determination of $A = -c$, through (2.7). This is consistent with the value plotted in figure 2 for $\lambda = \frac{1}{2}$, allowing for the uncertainty in the position of the lip. On the left of figure 4, we note the rapid decay of the disturbance both outside and inside the pipe. The infinite slope of the curves for $r = 1+$ and $1-$ on the downstream side of the lip shows that the curvature of the meridional sections of the vortex sheet is

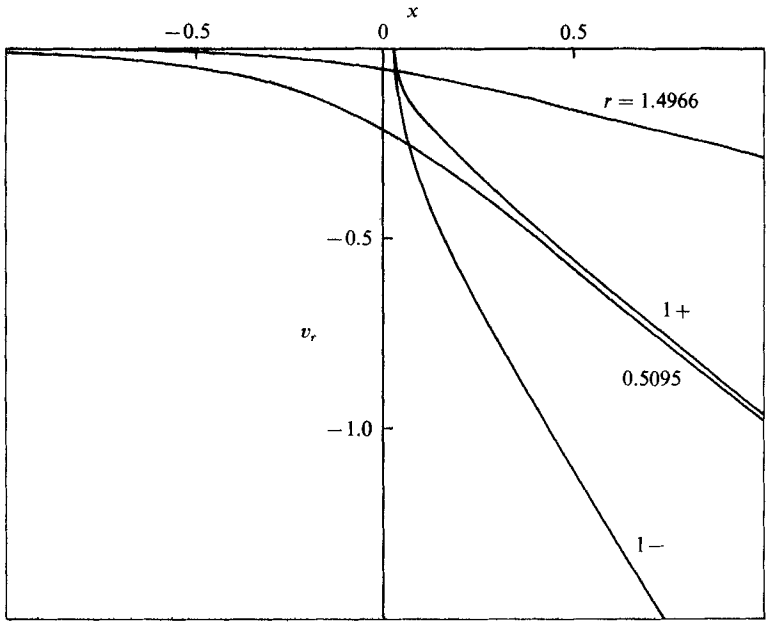

FIGURE 4. Radial component v_r of disturbance velocity for $\lambda = \frac{1}{2}$ near the orifice at various distances, r, from the axis.

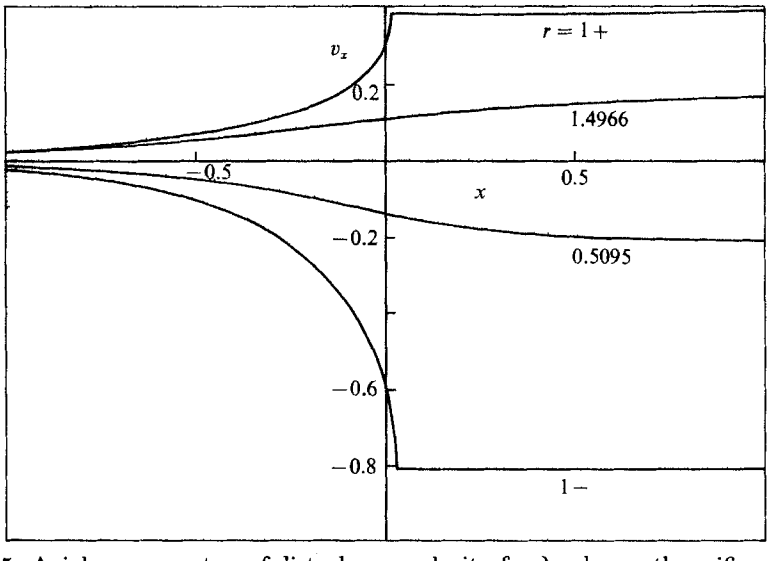

FIGURE 5. Axial component v_x of disturbance velocity for $\lambda = \frac{1}{2}$ near the orifice at various distances, r, from the axis.

infinite at the lip, except where $\cos 2\theta = 0$. This represents a significant departure, due to a term $O(\epsilon^2 x^{\frac{3}{2}})$ for $x \ll 1$, from the finite curvature of the vortex sheet in the far-field determined from (2.3).

In the same way, referring to (I3.23) and (2.12), we can write the axial component of the disturbance velocity in the near field as

$$\epsilon^2 v_x(r, x) \cos 2\theta, \tag{4.2}$$

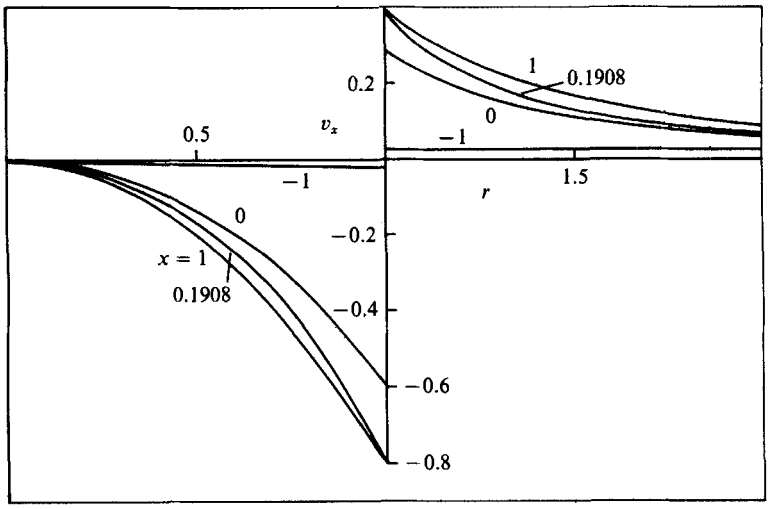

FIGURE 6. Axial component v_x of disturbance velocity for $\lambda = \frac{1}{2}$ at various axial stations, x, near the orifice.

where the leading term is unity inside the pipe and jet, and $\lambda\,(=\frac{1}{2})$ outside. v_x is shown in figure 5 as a function of x for the same four values of r. We see at once that the axial velocity is increased outside the pipe and jet in the windward and leeward quadrants and decreased in the lateral quadrants. This is what would be expected from the lateral flattening of the jet. Inside the pipe and the jet the sign of the disturbance velocity is reversed, which is also consistent with this jet deformation. The asymptotic behaviour, constant for v_x in accordance with (2.7), is reached quickly. Indeed, on the vortex sheet the asymptotic level is closely approximated at the lip, apparently driven by the need to satisfy the kinematic boundary condition (I3.28*b*) on the vortex sheet. On the left of the figure, the decay inside the pipe is rather more marked than that outside. The infinite slopes of the curves for $r = 1+$ and $1-$ represent an infinite acceleration of the fluid on the outside of the pipe and an infinite deceleration on the inside, for $\cos 2\theta > 0$. These arise from the infinite curvature of the vortex sheet discussed above in relation to figure 4. Comparing the curve for $r = 1-$ with figure 3, we see that the effect of a change in λ on the flow inside the pipe is primarily a change of scale. In each case, by $x = -0.5$ the disturbance velocity has fallen to about 12% of its maximum value, and by $x = -1$ to about 0.3%. The scale is determined, in terms of λ, by the asymptotic behaviour (2.7).

The dependence of v_x on r is illustrated in figure 6 for four values of x: -1 (upstream of the orifice), 0 (at the orifice), 0.1908 (near the orifice on the downstream side) and 1 (downstream of the orifice). $|v_x|$ decreases away from the cylinder $r = 1$ in both directions. Inside it falls to zero like r^2 as the axis is approached. At the upstream station the decay outside the pipe is very slow, but the level is low. The profiles at $x = 0.1908$ are more concave than those at $x = 1$, because the levels at $r = 1+$ and $1-$ are maintained, as discussed in relation to figure 5, and the smaller disturbance levels upstream of the orifice influence the values at the intermediate values of r. The profiles for $x = 0$ do not show this concavity because the solution there is affected by the finite mesh interval.

The result without the Kutta condition, as given in I and evaluated numerically

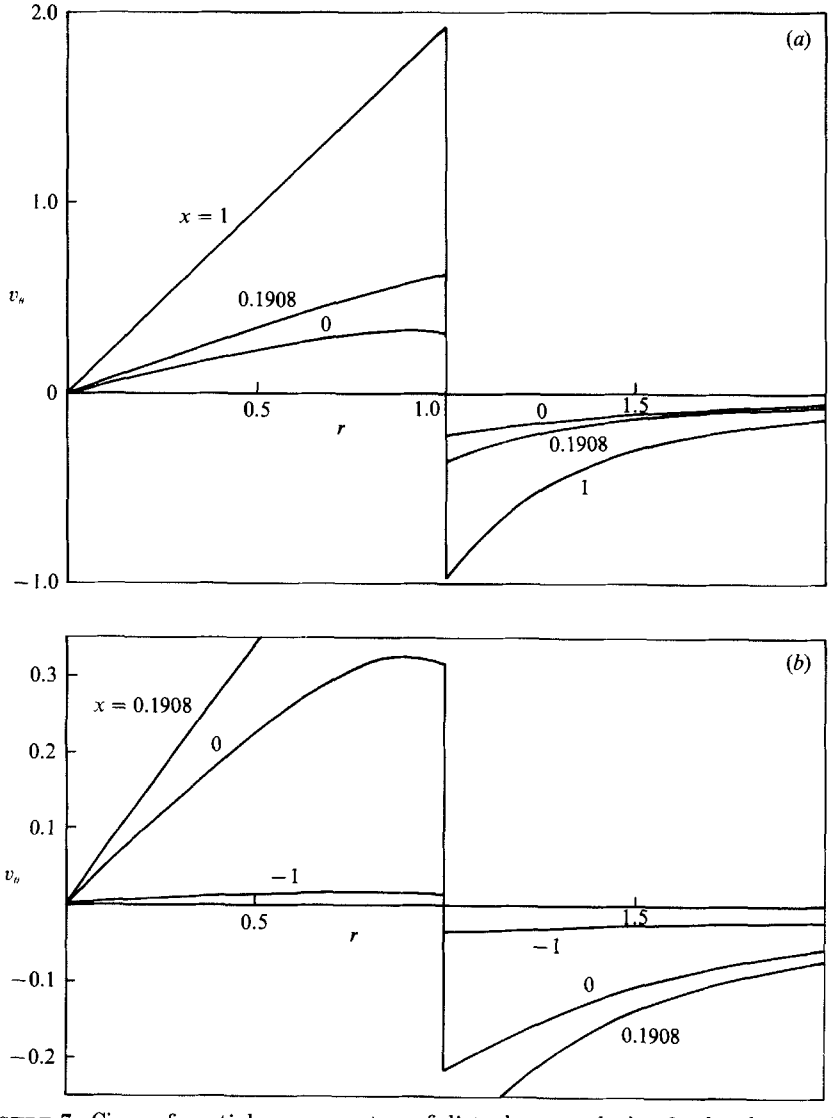

FIGURE 7. Circumferential component v_θ of disturbance velocity for $\lambda = \frac{1}{2}$ at various axial stations, x, near the orifice: (*a*) $x = 0, 0.1908, 1$. (*b*) $x = -1, 0, 0.1908$.

by Lytton & Smith (1988), shows the same asymptotic behaviour at large distances from the orifice, but exhibits the expected square-root singularity at the lip. v_r tends to infinity through positive values as the lip is approached along the jet boundary, $r = 1\pm, x > 0$; while v_x tends to infinity through positive values as the lip is approached along the inside of the pipe, $r = 1-, x < 0$, and through negative values on the outside of the pipe, $r = 1+, x < 0$.

From (I3.23) and (I3.13), the third, circumferential, component of velocity has a leading term $-\epsilon(1+r^{-2})\sin\theta$ outside the pipe and jet, corresponding to the flow round a circular cylinder. The next term can be written as

$$\epsilon^2 v_\theta(r, x)\sin 2\theta. \tag{4.3}$$

The variation of v_θ with r for $x = -1, 0, 0.1908$ and 1 is displayed in figures 7 (*a*) and 7 (*b*), where the change in scale is needed to show the behaviour at both $x = -1$ and $+1$. The most striking feature of figure 7 (*a*) is the linear variation of v_θ with r inside the jet at $x = 1$. This agrees with the asymptotic behaviour implied by (2.7) to within the uncertainty in the lip position. It represents the circumferential velocity which corresponds, on a planar flow basis, to the radial inflow along $\theta = 0$ and π and outflow along $\theta = \pm\frac{1}{2}\pi$. The profile outside the jet at $x = 1$ is nearly as close to the corresponding asymptotic behaviour given by (2.7). Even at $x = 0.1908$, the levels of v_θ at $r = 1$ are very close to their asymptotic values, though the profiles are somewhat distorted by the proximity of the orifice. In figure 7 (*b*) we notice particularly that v_θ reaches a maximum within the pipe. Its radial derivative should also vanish on the pipe wall, as it is seen to do at $x = -1$, though the numerical treatment fails to enforce the behaviour at the lip. The rate of decay of v_θ outside the pipe falls off upstream, like that of v_x in figure 6.

A final comment is based on the numerical values of the functions in figures 4–7. These all lie between ± 2. Consequently, if ϵ is restricted to the level of about 0.1 for which we should expect the small disturbance assumptions to be justified, the contribution to the velocity field from the terms $O(\epsilon^2)$ in (I3.23) remains small in the near field, similarly, since $c < 1$ in the range $0 \leqslant \lambda \leqslant 1$, the additional term introduced into the outer solution (2.1)–(2.3) also remains small. It follows that the near field; similarly, since $c < 1$ in the range $0 \leqslant \lambda \leqslant 1$, the additional term convective velocity in it, and figure 4 of I remains a valid representation. Apart from its principal role in reconciling the larger-scale solution with the pipe geometry, the near-field solution is significant in several respects. We have already mentioned how it determines the origin shift, c, and its introduction of an infinite curvature in the vortex sheet. It also affects the pressure variation to leading order. We find, from Bernoulli's equation, for the near-field behaviour:

$$\left.\begin{aligned} p - p_\infty &= -\epsilon^2\left(\frac{1}{2r^4} - \frac{\cos 2\theta}{r^2} + \lambda v_x \cos 2\theta\right) \quad \text{for} \quad r \geqslant 1, \\ \tilde{p} - p_\infty &= -\epsilon^2(\tfrac{1}{2} + v_x \cos 2\theta) \quad \text{for} \quad r \leqslant 1. \end{aligned}\right\} \tag{4.4}$$

However, we have seen that, on the jet, v_x reaches its asymptotic value immediately downstream of the orifice, so the jet pressures as calculated from the larger-scale solution in I remain correct.

5. Conclusions

(*a*) The solution obtained in I has been modified so as to satisfy a Kutta condition of smooth outflow at the pipe lip.

(*b*) The effect of this modification on the larger-scale flow is simply an upstream shift of its effective origin by about a quarter of the pipe radius.

(*c*) The complicated expressions representing the disturbance potential in the pipe and in the jet near the orifice have been shown numerically to join continuously and smoothly at the orifice.

(*d*) Comparison with the origin shift calculated by Coelho & Hunt (1989) for $\lambda = 0$ shows that the reservation expressed in I about the applicability of the Wiener–Hopf technique for values of λ too far from unity is unnecessary in the range, $0 \leqslant \lambda \leqslant 1$, of most relevance.

(*e*) The disturbance to the flow inside the pipe, shown in I to decay exponentially with distance upstream, is found numerically to be very small at a distance of one pipe radius from the orifice.

(*f*) The disturbance to the larger-scale flow in and outside the jet due to the presence of the orifice also decays almost completely within one pipe radius downstream of it.

(*g*) Satisfying a Kutta condition at the lip of the pipe makes a qualitative difference to the flow pattern near the lip. Numerical calculations based on I and presented in Lytton & Smith (1988) show streamlines negotiating the lip from the jet to the outer surface of the pipe over the forward and rearward quadrants and from the outer flow to the inside of the pipe over the lateral quadrants. This predicted behaviour, which does not represent that of a real fluid, is now replaced by a smooth departure of the streamlines from the lip of the pipe.

(*h*) For the small values of ϵ for which the small-disturbance approach is likely to be valid, the effect of the near-field solution on the velocity field is very small, and the figures reproduced in I remain representative.

This work has been carried out with the support of the Procurement Executive, Ministry of Defence.

REFERENCES

Coelho, S. L. V. & Hunt, J. C. R. 1989 The dynamics of the near field of strong jets in crossflows. *J. Fluid Mech.* **200**, 95–120.

Lytton, C. C. 1987 Solution of the Euler equations for transonic flow over a lifting aerofoil. *J. Comput. Phys.* **73**, 395–431.

Lytton, C. C. & Smith, J. H. B. 1988 Numerical evaluation of a solution representing a jet in cross-flow. *RAE Tech. Memo. Aero.* 2137, 38 pp.

Needham, D. J., Riley, N. & Smith, J. H. B. 1988 A jet in crossflow. *J. Fluid Mech.* **188**, 159–184.